Available online at www.sciencedirect.com

SCIENCE DIRECT®

Journal of volcanology and geothermal research

ELSEVIER

Journal of Volcanology and Geothermal Research 142 (2005) 173–191

www.elsevier.com/locate/jvolgeores

Rheology of welding: inversion of field constraints

James K. Russell*, Steven L. Quane

Igneous Petrology Laboratory, Department of Earth and Ocean Sciences, University of British Columbia, Vancouver, British Columbia, Canada V6T 1Z4

Received 25 January 2004; accepted 8 October 2004

Abstract

At present the mechanisms and rheological behaviour of pyroclastic deposits during welding and compaction are poorly understood. Here, we explore the extent to which the rheological properties of pyroclastic deposits are constrained by physical property distributions in welded ignimbrite. Physical properties of samples from a 20-m section of the Bandelier Tuff, New Mexico are used as proxies for strain. The observed strain (ε_T) is ascribed to a combination of a time-dependent viscous compaction (ε_v) and a time-independent mechanical compaction (ε_m) described by:

$$\varepsilon_T = \frac{(1-\phi_o)}{\alpha}\ln\left\{1+\frac{\alpha\sigma\Delta t}{\eta_o(1-\phi_o)}\exp^{\frac{\alpha\phi_o}{(1-\phi_o)}}\right\}+\frac{\sigma}{E(1-\phi_o)}$$

where ϕ_o is the original porosity, σ is load, and η_o and E are the viscosity and Young's modulus of the deposit at zero porosity, respectively. The quantity α is an experimentally determined parameter used to relate the viscosity and porosity of porous aggregates. Simple conductive heat transfer models are used to generate cooling curves for individual samples; these curves dictate times of residence (Δt) at temperatures above the glass transition temperature. We adopt an inverse model approach whereby the observations on the natural material and model cooling curves are used to constrain the values of η_o ($10^{14.5}$ Pa s) and E (3–7 MPa). Our optimization also predicts the relative components of viscous and mechanical compaction throughout the welded ignimbrite. Viscous compaction dominates the lower two thirds of the section (ε_v: ε_m>1.0); the maximum in ε_v is coincident with the observed peak in welding intensity. Lastly, we present two dimensionless numbers (Q_A and Q_B) which are used to create a map of welding potential for pyroclastic deposits. The map has four quadrants which coincide with (i) no welding, (ii) welding and compaction driven by temperature (ε_v>ε_m) or (iii) by gravitational loading (ε_m>ε_v), and (iv) welding aided by temperature and load ($\varepsilon_v \cong \varepsilon_m$).

Keywords: welding; ignimbrite; rheology; inverse model; strain; physical properties

* Corresponding author. Tel.: +1 604 822 2703; fax: +1 604 822 6088.
E-mail address: krussell@eos.ubc.ca (J.K. Russell).

0377-0273/$ - see front matter © 2004 Elsevier B.V. All rights reserved.
doi:10.1016/j.jvolgeores.2004.10.017

1. Introduction

At present the mechanisms, controls, and time-scales of welding processes in volcanology are poorly understood. There are, for example, few experimental data that elucidate the rates, mechanisms, or rheology of compaction in pyroclastic mixtures (e.g., Boyd, 1961; Friedman et al., 1963; Bierwirth, 1982; Quane, 2004; Grunder et al., 2005—this issue; Quane and Russell, 2005—this issue). Here, we explore the extent to which physical property data from welded ignimbrite, serving as proxies for strain, can be used to constrain the rheological properties of the deposit during the welding process.

Welding of pyroclastic deposits involves the sintering of hot glassy particles (Smith, 1960a; Guest and Rogers, 1967; Ragan and Sheridan, 1972; Sparks and Wright, 1979) and is greatly facilitated when emplacement temperatures exceed the glass transition temperature (T_g) of the juvenile volcanic material (e.g., Riehle et al., 1995; Giordano et al., 2000, 2005—this issue). Welding is commonly accompanied by compaction resulting from gravitational loading. Although compaction is a response to load, the extent of compaction is strongly controlled by the viscosity (hence temperature) of the deposit. Under the right conditions, substantial compaction can occur in relatively thin (<10 m) deposits, such as described in proximal air-fall deposits (e.g., Sparks and Wright, 1979; Kamata et al., 1993) or in spatter flows (Gottsmann and Dingwell, 2001).

Compaction can be viewed as operating via two end-member processes. At one end of the spectrum, compaction involves the mechanical rearrangement of particles that essentially behave as solids (e.g., Sheridan and Ragan, 1976; Sheridan and Wang, 2005—this issue). Mechanical compaction strongly depends on the magnitude of gravitational loading, but operates to some extent in all pyroclastic deposits, even those that are emplaced at or below T_g. On the other hand, compaction also proceeds through the permanent viscous deformation of hot clasts or particles that are basically fluids. Viscous compaction is responsible for the efficient sintering and collapse of glassy shards and pumiceous lapilli in ignimbrite deposits (i.e., Smith, 1960a; Guest and Rogers, 1967). Both mechanical and viscous compaction lead to reduction of primary porosity, densification, and the development of planar fabric (e.g., eutaxitic texture) oriented perpendicular to the lithostatic load (e.g., Smith, 1960a; Ross and Smith, 1961; Sheridan and Ragan, 1976; Streck and Grunder, 1995; Kobberger and Schmincke, 1999).

Below, we use the physical properties of samples from a section of the Bandelier Tuff, New Mexico, to constrain the rheology of the deposit during the welding and compaction. The physical properties provide a quantitative record of total strain ascribed to welding and compaction as a function of depth (e.g., Ragan and Sheridan, 1972; Sheridan and Ragan, 1976; Peterson, 1979; Kobberger and Schmincke, 1999). These observations are coupled to transient conductive cooling models which provide the thermal history for individual samples (e.g., Riehle, 1973; Miller, 1990; Riehle et al., 1995; Kobberger and Schmincke, 1999). The unknowns in the problem are the viscosity and Young's modulus of the framework material in a generalized relationship for mechanical and viscous compaction of pyroclastic deposits. Inversion of the natural dataset provides a constitutive relationship that predicts strain as a function of load, porosity, viscosity (e.g., temperature), and time which can be used to investigate the mechanisms and time-scales of welding and compaction in pyroclastic deposits.

2. Field and laboratory measurements

Our analysis is based on material collected from the Bandelier Tuff, a Pleistocene rhyolite ash-flow sequence in the Jemez Mountains of northern New Mexico (Smith and Bailey, 1966). The pyroclastic succession has two main members: a single cooling unit called the Otowi member, and the overlying Tshirege member which comprises four distinct cooling units (Broxton and Reneau, 1995). Our study uses samples of rock cores recovered from four drill holes (Fig. 1; SCC-1, SCC-2, SCC-4 and NISC-2) that completely penetrate Unit 4 of the Tshirege member (e.g., Smith and Bailey, 1966; Vaniman and Wohletz, 1990, 1991; Goff, 1995). At this location, Unit 4 comprises a 20-m-thick single cooling unit of ignimbrite, underlain by a crystal-rich co-ignimbrite surge deposit (Krier et al., 1998).

The ignimbrite varies in welding intensity from non-welded to partially welded (Broxton and

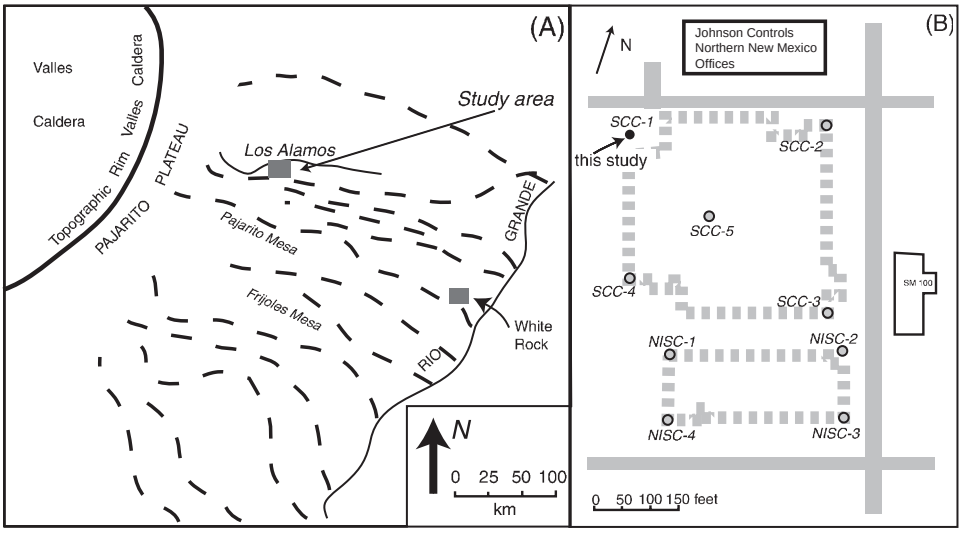

Fig. 1. Geographic map showing locations of drill holes in Bandelier Tuff from which samples of core were collected for this study. (A) Plan view of geographic context relative to Valles Caldera. Area is underlain by Bandelier Tuff and dashed lines denote prominent canyons which dissect and provide exposure through the ignimbrite. (B) Detailed plan view map of borehole locations relative to existing and proposed (dashed lines) buildings belonging to Los Alamos. This study uses data collected from core samples from borehole SCC-1.

Reneau, 1995; Krier et al., 1998). The density, porosity and degree of flattening of pumice lapilli vary continuously with depth in each section suggesting a single cooling unit. Quane and Russell (2004) measured physical properties on samples from these cores to track variations in welding intensity within the Bandelier Tuff. The measurements included density, porosity and textural traits (e.g., fabric angle, flattening ratios) and the data collected from the most complete section (SCC-1) are reproduced in Table 1 and plotted against depth in Fig. 2. Using Quane and Russell's (2004) scheme for rating welding intensity, the samples of Bandelier Tuff from section SCC-1 have Ranks of II and III (Table 1; Fig. 2D). Rank II samples comprise largely undeformed ash and pumice lapilli but have good cohesion indicative of incipient welding or sintering (e.g., Peterson, 1979; Streck and Grunder, 1995; Wilson and Hildreth, 2003. In Rank III samples both the ash matrix and pumice lapilli are deformed, but there is insufficient strain to produce a eutaxitic texture (e.g., partial or poorly welded; Smith, 1960b; Wilson and Hildreth, 2003). None of the samples were assigned a Rank of I; such samples are unconsolidated and undeformed (e.g., unwelded; Smith, 1960b; Peterson, 1979).

Bulk densities were measured using conventional hydrostatic weighing techniques after coating with Krylon Crystal Clear© aerosol to make them impermeable to water. Calculated densities were corrected for water temperature; the mass and volume of Krylon© proved to be negligible (Quane and Russell, 2004). Replicate analyses suggest that density measurements (Fig. 2A) have a relative precision (1σ) of <0.1%.

Pore space in all samples was measured by helium pycnometry and has an 1σ analytical precision of 1%. Pycnometry experiments directly measure the volume of the sample; this volume includes the framework (solid) material, as well as, the volume of pores that are isolated within the sample (e.g., pores that are inaccessible to the gas). Our reported values of porosity (e.g., Table 1; Fig. 2B) assume that all pores are connected and, thus, are minimum estimates. This assumption is justified more fully below (i.e., Fig. 3).

Textural variations between samples were measured in two ways. Firstly, welding in pyroclastic deposits causes ash shards to flatten and rotate perpendicular to the loading direction creating a planar fabric (e.g., Smith, 1960a,b; Smith and Bailey, 1966; Sheridan and Ragan, 1976; Smith, 1979;

Table 1
Physical properties of samples from a 20-m-thick section of Bandelier Tuff (SCC-1), including: current depth (m), density (ρ), fractional porosity (ϕ), particle alignment (mean angle), and flattening of pumice lapilli (e.g., c/a; height/length ratios of fiamme)

Depth	ρ	ϕ	Mean angle (°)	Fiamme c/a	ε (ρ)	ε (ϕ)	Oblateness[a]	Strain[b]	Rank[c]
0.00	1.268	0.511	53.58	0.597	0.080	0.080	0.403	0.046	II
1.30	1.321	0.493	45.53	0.577	0.117	0.118	0.423	0.060	II
2.36	1.336	0.489	44.86	0.579	0.126	0.118	0.421	0.070	II
3.51	1.356	0.480	37.89	0.563	0.139	0.135	0.437	0.081	II
3.89	1.378	0.470	45.17	0.460	0.153	0.151	0.540	0.084	II
4.73	1.401	0.464	42.83	0.479	0.167	0.160	0.521	0.092	II
5.64	1.442	0.448	42.84	0.487	0.191	0.185	0.513	0.101	II
6.55	1.450	0.455	39.99	0.450	0.195	0.174	0.550	0.109	II
7.62	1.497	0.425	40.01	0.430	0.220	0.217	0.570	0.119	II
8.23	1.520	0.416	43.58	0.411	0.232	0.231	0.589	0.124	II
8.99	1.534	0.408	–	0.423	0.239	0.240	0.577	0.131	II
9.91	1.572	0.392	38.50	0.421	0.258	0.260	0.579	0.138	II
11.81	1.588	0.388	40.23	0.388	0.265	0.265	0.612	0.154	II
12.42	1.642	0.364	38.24	0.401	0.289	0.294	0.599	0.159	II
13.57	1.701	0.341	28.80	0.323	0.314	0.317	0.677	0.169	II
16.92	1.802	0.299	29.42	0.312	0.352	0.358	0.688	0.196	III
17.45	1.783	0.308	34.23	0.346	0.345	0.350	0.654	0.199	III
18.06	1.725	0.331	39.02	0.358	0.323	0.327	0.642	0.203	III
18.75	1.603	0.383	36.53	0.378	0.272	0.271	0.622	0.206	II
19.44	1.590	0.383	36.26	0.550	0.266	0.271	0.450	0.208	II
Average	1.526	0.412	–	–	0.227	0.226	0.553	0.132	–

Includes calculated values of strain (ε) based on sample density (ρ), fractional porosity (ϕ), and oblateness computed from dimensions of flattened pumice lapilli. Calculations use a matrix density of 2.594 g cm^{-3} (measured values 2.574 g cm^{-3}) and a minimum original porosity of 55% implying an original density for the deposit of 1.1675 g cm^{-3} (see text).

[a] Oblateness is an average value of $(1-c/a)$ for 20 or more pumice lapilli per sample.

[b] Integrated strain down section (see text).

[c] Rank of individual samples is based on classification of Quane and Russell (2004).

Peterson, 1979). The intensity of this fabric was tracked by measuring the mean orientation of glass shards (horizontal taken as 0°) from digital images created by scanning entire polished sections. Tracings were made of select ash shards (N>100 per sample) within the matrix and image analysis was used to calculate a mean angle (Table 1). Shards commonly show enhanced alignment or deformation when they

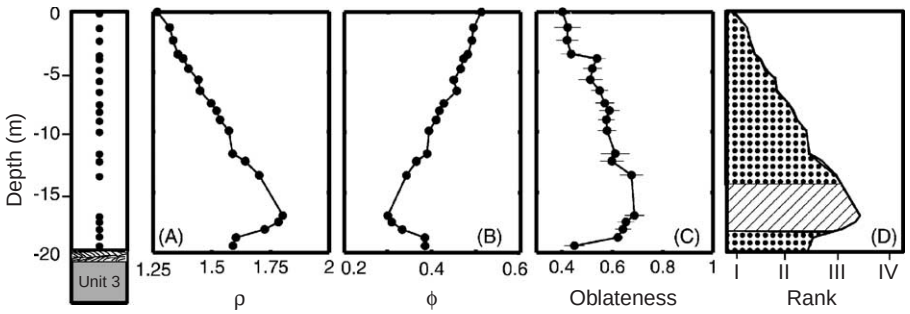

Fig. 2. Physical properties of samples (Table 1) collected from 20-m-thick section of the Bandelier Tuff (left side panel) are plotted against depth (m), including: (A) density (ρ; g cm^{-3}), (B) fractional porosity (ϕ), and (C) oblateness of pumice lapilli. All metrics vary systematically with depth and define maxima or minima between depths of 13 and 17 m. Error bars denote 1σ measurement uncertainties for oblateness; corresponding uncertainties on ρ and ϕ are smaller than symbols. (D) Stratigraphic variation in welding intensity described by values of rank after Quane and Russell (2004,2005—this issue).

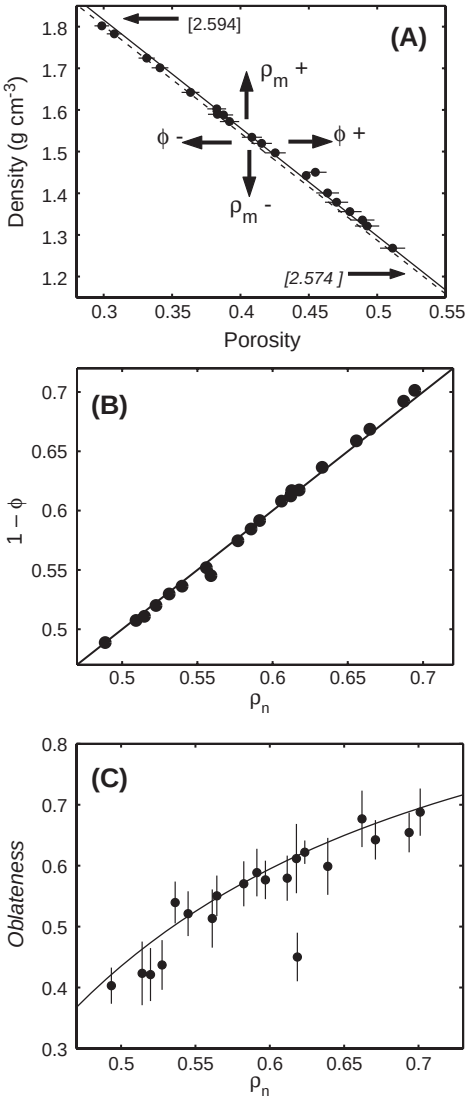

Fig. 3. Covariance of physical property measurements. (A) Measured values of density plotted against porosity and compared to model lines for a constant matrix density (ρ_m) of 2.574 (measured) and 2.594 (fitted). Arrows show effects of variations in ρ_m or isolated porosity (see text). (B) Porosity as $(1-\phi)$ is plotted against density normalized to ρ_m (2.594). Solid line denotes model 1:1 relationship. (C) Values of oblateness derived from measurements of flattened pumice lapilli increase non-linearly against ρ_n. Error bars are as discussed in Fig. 2.

are near phenocrysts, therefore, measurements were made only on shards that were well-removed from the margins of crystal. The mean angle and the variance on the fabric angle decrease as welding intensity increases (e.g., Sparks and Wright, 1979; Ragan and Sheridan, 1972; Quane and Russell, 2004).

Secondly, pumice lapilli deform to form flattened ellipsoids during welding. Sheridan and Ragan (1976) demonstrated on samples of Bishop Tuff and Aso 4 Tuff that, during deformation of lapilli, the horizontal axes (a and b) change equally as the vertical axis (c) shortens. The progressive deformation of pumice lapilli (e.g., fiamme) is, therefore, fully characterized by measurements of length (a) and height (c) taken perpendicular to the flattening direction (Dunnet, 1969; Sheridan and Ragan, 1976; Peterson, 1979; Sparks and Wright, 1979) after correcting for any original particle elongation (e.g., Sheridan and Ragan, 1976; Sparks and Wright, 1979). Table 1 lists the average (N>20) height to length ratios (c/a) of fiamme for each sample in section SCC-1.

Density serves as a proxy for porosity if the matrix has a constant density (ρ_m) and all porosity is connected. In such situations, the two properties are exactly related by:

$$\rho = [1 - \phi]\rho_m. \quad (1)$$

The range of ρ_m values calculated from measured values of porosity for the 20 samples listed in Table 1 is 2.56–2.61 g cm^{-3}. Two model lines are compared to the data from the Bandelier Tuff (Fig. 3A). One model uses the average matrix density (2.57±0.01) derived from helium pycnometry measurements of powdered samples, whereas the other was obtained by fitting Eq. (1) to the entire dataset for an optimum value of ρ_m (2.59).

The slight discrepancies between the preferred model line and the SCC-1 dataset (Table 1) are non-systematic and have several explanations (see arrows in Fig. 3A). In situations where the measured porosity actually represents total porosity, variations in matrix density (e.g., variations in percent crystals) can cause data to drift above (higher ρ_m) or below (lower ρ_m) the model line. The presence of isolated pore space would cause data to plot to the left of the model line (Fig. 3A). Scatter to the right (higher porosity) is most easily ascribed to higher values of ρ_m. Fig. 3B shows density (ρ_n) normalized to the average matrix density plotted against $(1-\phi)$. Except for a single sample, the dataset is within experimental uncertainty of the 1:1 relationship expected if the matrix

density is essentially constant (2.59 g cm^{-3}) and all porosity is connected.

Values of oblateness are calculated for individual samples from measured ratios of axial lengths (a) and heights (c) on flattened pumice lapilli as $[1-c/a]$ (Table 1). Oblateness increases with intensity of welding and shows a non-linear dependence on normalized density (Fig. 3C).

3. Metrics of strain

The physical property dataset tracks strain accumulated during welding and compaction of the Bandelier Tuff (e.g., Smith and Bailey, 1966; Ragan and Sheridan, 1972; Sheridan and Ragan, 1976; Peterson, 1979; Sparks and Wright, 1979; Kobberger and Schmincke, 1999). Strain is manifest by shortening of the original deposit thickness ($\Delta L/L_o$) mainly through porosity loss (e.g., volume strain; Fig. 4). The porosity loss is accommodated by compaction and deformation of the ash-rich matrix and pumiceous particles (e.g., lapilli and blocks), respectively. Thus, progressive strain is attended by densification (e.g., Sheridan and Ragan, 1976; Streck and Grunder, 1995), flattening of pyroclasts (e.g., Peterson, 1979; Sparks and Wright, 1979), and increasing rock cohesion (e.g., Quane and Russell, 2003). The spatial variation of these physical properties has been used to constrain the thermal history of pyroclastic deposits (e.g., Riehle, 1973; Riehle et al., 1995; Kobberger and Schmincke, 1999), but can also be used to constrain the rheology of the welding process.

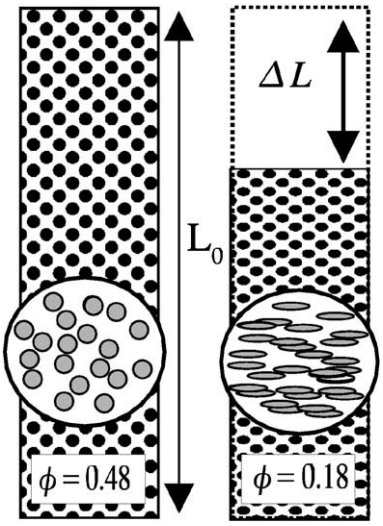

Fig. 4. Schematic representation of volume strain in welded pyroclastic deposit. Original pyroclastic deposit has thickness L_0 and fractional porosity of 0.48. Strain attending welding process is manifest as shortening of section (ΔL), reduction of porosity (e.g., 0.18), and flattening of particles.

Lithostatic loads are calculated for the entire section of Bandelier Tuff (SCC-1) using measured values of bulk density (Fig. 5A). The maximum load at the base of the cooling unit is at least 0.3 MPa. The magnitude of the effective lithostatic load for each sample is constant throughout welding unless porosity becomes isolated. A substantial isolated porosity could sustain an internal fluid pressure which would reduce the total lithostatic load (e.g., Friedman et al., 1963; Bierwirth, 1982; Sparks et al., 1999; Grunder and Russell, 2005—this issue). There is no measurable isolated porosity in our samples of Bandelier Tuff which argues against the development of internal fluid pressure during welding. If there were isolated, fluid-filled pores in the early stages of welding and compaction, the fluids must have escaped or been absorbed by the melt (Sparks et al., 1999) early enough in the process to permit the complete collapse of the pores.

Values of strain (Fig. 5B) are calculated assuming a matrix density of 2.59, an original porosity (ϕ_o) of 55%, and pure volume strain using measurements of porosity:

$$\varepsilon(\phi) = \frac{(\phi_o - \phi)}{(1-\phi)}, \tag{2}$$

and density:

$$\varepsilon(\rho) = \frac{\rho - \rho_o}{\rho}. \tag{3}$$

Our estimate of ϕ_o is a conservative minimum; previous workers, using densities of welded, unwelded and powdered samples, have estimated ϕ_o for the Bandelier Tuff at 53% to 60% ((Riehle et al., 1995; Wilson and Hildreth, 2003; Sheridan and Wang, 2005—this issue). The values of strain derived from bulk density and porosity measurements are virtually identical (Table 1; Fig. 5B).

Under the condition of pure volume strain, particle oblateness is also a measure of total strain if the original shapes were spherical (Table 1). The values of

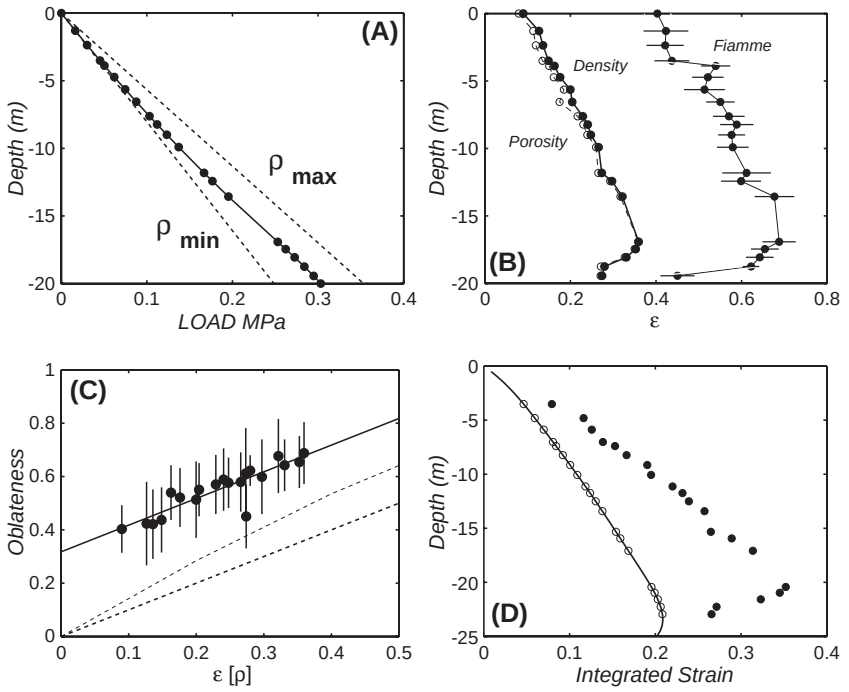

Fig. 5. Physical properties of Bandelier tuff samples and the implied strain equivalence. (A) Lithostatic load calculated from values of ρ vs. depth (m). Solid curve is load calculated by integration of curve fitted to density profile (e.g., Fig. 2A); dashed lines are loads implied by most and least dense samples. (B) Values of strain calculated from measurements of density, porosity, and flattening of fiamme vs. depth. (C) Strain computed from density vs. measured values of oblateness. Solid curve suggests flattening of pumice lapilli via coaxial, volumetric strain; *Y*-intercept constrains the original particles to a height to length ratio of 0.67 (e.g., 1.5 times elongation). Dashed lines are for a sphere undergoing volume strain (e.g., porosity loss; heavy-dash) or pure shear strain (e.g., constant volume; light-dash). (D) Integrated strain for the section restored to its complete (23 m) thickness (open circles with line) is compared to strain recorded by individual samples (solid circles).

strain calculated from the oblateness of fiamme record a similar pattern with depth as displayed by $\varepsilon(\phi)$ and $\varepsilon(\rho)$, but are displaced to higher values (Fig. 5B). This discrepancy could result from an original (pre-welding) alignment of pumice lapilli (e.g., Elliot, 1970; Sheridan and Ragan, 1976; Sparks and Wright, 1979). Fig. 5C compares the strain computed from density to oblateness of fiamme. The dashed lines show two ideal end-member relationships. Under the conditions of pure volume strain, all strain is accommodated by volume loss and deformed particles must lie along the heavy-dashed line which describes a 1:1 relationship between $\varepsilon(\rho)$ and oblateness. Under conditions of pure shear (volume conservation) deformed materials would lie along the curvilinear light-dashed line. Along this path, a fixed value of strain requires particles to show a greater oblateness because volume is conserved. Compaction of pyroclastic deposits is largely controlled by porosity loss (volume strain) and the data collected from the Bandelier Tuff (solid dots; Fig. 5C) are consistent with pure volume strain if the average lapilli had an original length/height ratio of 1.5 (intercept value). Alignment of elongate pyroclasts parallel to the ground surface is common in pyroclastic deposits (Ross and Smith, 1961; Sheridan and Ragan, 1976; Peterson, 1979; Sparks and Wright, 1979; Kobberger and Schmincke, 1999).

The maximum value of strain is just over 35% (Table 1); the minimum values are 7–8%, suggesting that a small portion ($\cong$5 m) of the upper section is missing. Consequently, all subsequent calculations (e.g., depth, load, etc.) are made assuming a post-welding thickness of 23 m (Table 3). The strain recorded by each sample of Bandelier Tuff can be used to estimate the total strain in the section. We calculated the cumulative strain with depth by fitting the $\varepsilon(\rho)$–depth dataset to a polynomial and then integrating the function over the full (23 m) section

(Fig. 5D). Although individual samples (●) record up to 36% strain, the entire section represents a maximum strain of 21% strain (Table 1) suggesting an overall shortening of 5–7 m and original pre-welding thickness of 28–30 m.

4. Thermal model

The physical property variations within the ignimbrite record the strain accumulated during welding and compaction. The duration of this process is limited by the cooling history of the deposit. Our aim is to use the observed distribution of strain (Fig. 5) and the thermal history of each sample, as predicted by a simple conductive cooling model, to constrain the rheological properties of the Bandelier Tuff during the welding process.

We adopt a one-dimensional, transient, heat conduction model to simulate the cooling history of the SCC-1 section of Bandelier Tuff. The model does not attempt to compete with more sophisticated forward models used to simulate simultaneous compaction and cooling of ignimbrite sheets (e.g., Riehle, 1973; Miller, 1990; Riehle et al., 1995; Sheridan and Wang, 2005—this issue), but is intended to provide a reasonable cooling history for this section of Bandelier Tuff. Most importantly, our model provides cooling history curves for individual samples based on their relative positions (depths), and we submit that the predicted "*differences*" between our model curves are robust.

We assume the ignimbrite is emplaced at a uniform temperature (T_e) and we use the upper limit of emplacement temperatures from Riehle (1973). This assumes *en masse* emplacement of the full thickness of ignimbrite or, if deposition was progressive (Branney and Kokelaar, 1992; Wilson and Hildreth, 2003), that the rates of aggradation were sufficiently high to prevent substantial cooling between depositional events (cf. Sheridan and Wang, 2005—this issue). The upper boundary cools to the atmosphere via natural convection assuming a constant air temperature (e.g., Riehle, 1973; Miller, 1990; Riehle et al., 1995). The base of the unit conducts heat to the ground which maintains a far-field temperature of 25 °C. The model does not incorporate phase changes or moving boundaries. The boundary value problem was solved with finite-difference using fixed step sizes. All model parameters and the sources used are summarized in Table 2.

The transient temperature distribution in the pyroclastic flow is shown for a total time of 7 years by plotting the temperature distribution in the ignimbrite and the underlying ground at increments of 3 months (Fig. 6A). Within three years the hottest portion of the body has cooled below 0.5 T_e, which agrees well with previously published models (e.g., Riehle, 1973; Miller, 1990; Riehle et al., 1995). The efficiency of natural convection on the upper boundary surface, relative to the base, causes the asymmetric temperature distribution. The conductive cooling model dictates that the lower contact is held near 400 °C for about 3 years.

The transient conductive cooling model provides individual cooling history curves for depths corresponding to each of the 20 samples collected from section SCC-1 of the Bandelier Tuff (Table 3; Fig. 6B). The cooling curves predict the time each sample would take to cool from T_e to some critical temper-

Table 2
Parameters used in finite difference model for conductive cooling of pyroclastic flow deposit

Parameter	Symbol	Value	Sources[a]
Emplacement temperature (°C)	T_e	825	N/A
Glass transition temperature (°C)[b]	T_g	650 (*D*)–508 (*W*)	N/A
Air temperature (°C)	T_a	25	N/A
Ground temperature (°C)	$T\infty$	25	N/A
Thickness (m)	L	25	7
Thermal conductivity (J m^{-1} K^{-1} s^{-1})	K	1.2	2, 3
Thermal diffusivity (m^2 s^{-1})	α	0.5×10^{-6}	2, 4, 5, 6
Free convection coefficient (J m^{-2} K^{-1} s^{-1})	h	10	1, 2, 3, 4
Grid step-size for position (m)	ΔZ	0.05	1, 3
Grid step-size for time (s)	Δt	5000	1, 3, 4, 5

See text for further explanation and discussion of boundary conditions.

[a] Sources include: (1) Carslaw and Jaeger (1959); (2) Riehle (1973); (3) Philpotts (1990); (4) Miller (1990); (5) Riehle et al. (1995); (6) Kobberger and Schmincke (1999); and (7) Quane and Russell (2004).

[b] Values of T_g are for Bandelier Tuff having 0 (*D*) or 2 (*W*) wt.% H_2O (see Fig. 7).

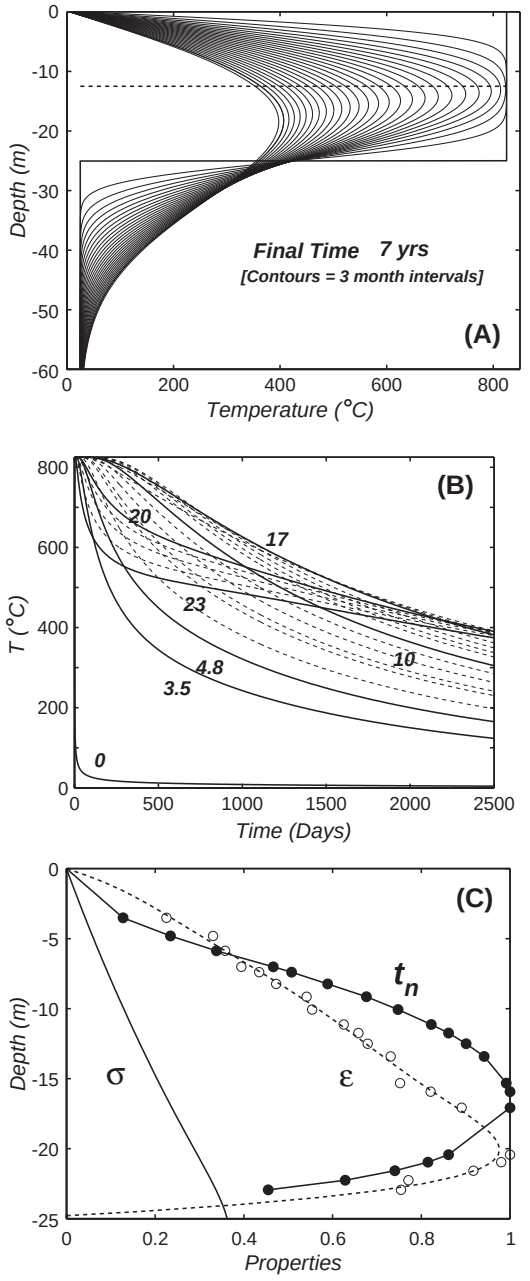

Fig. 6. Results of simplified conductive cooling model for pyroclastic flow deposit. (A) Temperature distributions in 25-m-thick deposit are shown during first 7 years cooling at 3-month intervals. (B) The model cooling curves (T °C vs. time) for specific depths corresponding to the samples of Bandelier tuff (Table 3). Labels are sample depths associated with heavy lines. (C) Summary of relationships between stratigraphic load (σ; MPa), strain recorded by individual samples (ε), and time of residence at T (°C)>Tg. Values of strain and residence time (t_n) are normalized.

ature where welding and compaction cease (e.g., T_g; see below). The total time (e.g., Δt_i) and the actual path taken are dependent on sample depth (see labels Fig. 6B). Logically, samples near the upper and lower surface cool rapidly, whereas samples from the interior portions of the ignimbrite cool over longer periods of time and have different T–t paths. Ultimately, we might expect that the intensity of welding should be proportional to the area under these curves and/or to the lithostatic load. The idea that welding is simply and universally proportional to these variables alone is tested in Fig. 6C. Lithostatic load (σ) increases nearly linearly with depth (Table 3; Fig. 6C) whereas the time of residence at temperatures $>T_g$ peaks two-thirds of the way down the section and maximum strain is found in samples 80–90% down the section. Although, the position of the peak residence time is somewhat dependent on the boundary conditions (e.g., Riehle, 1973; Miller, 1990; Riehle et al., 1995). Fig. 6C illustrates that the position of peak values of σ, ε, and t_r need not be coincident. This simple comparison highlights the possibility of complete or partial decoupling of load, residence time, and strain.

5. Residence times

The model cooling history curves (Fig. 6B) provide a means of estimating the time each sample spent at temperatures high enough to promote welding and compaction. Viscous compaction, in particular, will be most efficient at temperatures above the glass transition temperature (T_g) which corresponds to viscosities in the interval 10^{12}–$10^{12.5}$ Pa s (e.g., Dingwell and Webb, 1989, 1990; Kamata et al., 1993; Kobberger and Schmincke, 1999; Giordano et al., 2005—this issue). At temperatures below T_g, welding and compaction processes are limited because the time scales required for viscous relaxation increase to the point that they are comparable or longer than the timescales of cooling (e.g., Dingwell and Webb, 1989, 1990; Giordano et al., 2005—this issue).

We use the calculated temperature dependent viscosity curves (Shaw, 1972) for melt of the same composition as the Bandelier Tuff (Krier et al., 1998) to define the characteristic T_g. The appropriate viscosity curves are plotted in Fig. 7 for an

Table 3
Output from cooling model for revised sample depths, including: residence time above T_g (t), area under cooling curve (Area), and dimensionless numbers (Q_A and Q_B)

Present Depth (m)	Original Depth (m)	Load (MPa)	Anhydrous				Hydrous			
			t (days)	Area (°C s)	Q_A	Q_B	t (days)	Area (°C s)	Q_A	Q_B
–	0	0	0.1	0.0E+0	0.000	0.000	0.1	0.00E+00	0.000	0.000
0.00	3.51	0.0422	95.7	8.4E+8	0.156	0.108	206.6	2.7E+9	0.266	0.233
1.30	4.81	0.0585	173.8	1.6E+9	0.289	0.273	379.3	5.0E+9	0.492	0.596
2.36	5.87	0.0724	258.4	2.3E+9	0.425	0.504	547.0	7.3E+9	0.723	1.066
3.51	7.02	0.0875	366.2	3.3E+9	0.605	0.866	754.7	1.0E+10	1.015	1.785
3.89	7.40	0.0927	406.3	3.6E+9	0.674	1.019	821.5	1.1E+10	1.122	2.059
4.73	8.24	0.1041	500.3	4.5E+9	0.830	1.412	953.2	1.4E+10	1.351	2.689
5.64	9.15	0.1168	587.6	5.4E+9	1.001	1.862	1094.6	1.6E+10	1.587	3.470
6.55	10.07	0.1298	672.9	6.3E+9	1.167	2.371	1210.1	1.8E+10	1.805	4.264
7.62	11.13	0.1452	764.1	7.3E+9	1.345	3.013	1331.3	2.1E+10	2.034	5.250
8.23	11.74	0.1542	802.1	7.7E+9	1.423	3.358	1394.1	2.2E+10	2.137	5.837
8.99	12.50	0.1655	841.1	8.1E+9	1.498	3.781	1458.3	2.3E+10	2.243	6.555
9.91	13.42	0.1794	871.0	8.4E+9	1.547	4.243	1524.0	2.4E+10	2.330	7.424
11.81	15.32	0.2091	881.1	8.0E+9	1.490	5.006	1604.7	2.4E+10	2.359	9.118
12.42	15.93	0.2188	871.0	7.7E+9	1.418	5.183	1618.4	2.4E+10	2.318	9.630
13.57	17.08	0.2376	811.8	6.6E+9	1.232	5.248	1618.4	2.2E+10	2.180	10.463
16.92	20.43	0.2950	379.3	2.6E+9	0.473	3.051	1394.1	1.3E+10	1.322	11.212
17.45	20.96	0.3043	304.0	2.0E+9	0.376	2.522	1318.9	1.2E+10	1.143	10.941
18.06	21.57	0.3148	221.5	1.5E+9	0.273	1.901	1198.3	9.3E+9	0.918	10.281
18.75	22.26	0.3262	139.8	9.4E+8	0.174	1.243	1017.2	6.6E+9	0.647	9.045
19.44	22.95	0.3370	79.7	5.3E+8	0.097	0.733	736.1	3.9E+9	0.385	6.763

Values are for anhydrous and hydrous ignimbrite.

anhydrous and a hydrous version of the melt. On the basis of these calculated curves, the predicted T_g values differ by 140 °C depending on whether the melt is anhydrous (650 °C) or has 2 wt.% H_2O (508 °C). This difference in T_g translates into a substantial difference in the time of residence above T_g (Fig. 8; Table 3). Ignimbrites having lower water contents have higher T_g values, potentially smaller $T_e - T_g$ intervals, and, thus, less time for welding to occur.

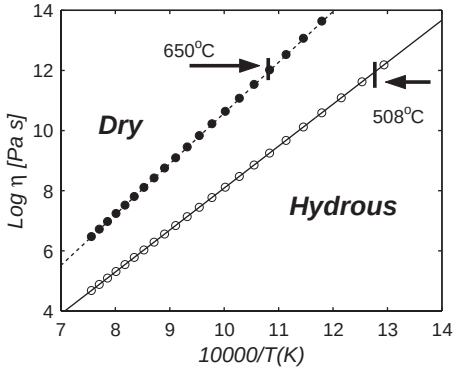

Fig. 7. Calculated viscosity curves for melt of the same composition as the Bandelier tuff (Krier et al., 1998) using the Shaw (1972) model. Calculated viscosity curves are for anhydrous melt (Dry: ●) and for melt with 2 wt.% H_2O (Hydrous: ○). Characteristic glass transition temperatures corresponding to a viscosity of 10^{12} Pa s are shown for both melt compositions.

We have created an objective measure of the residence time in the welding window (Fig. 8A) by computing the area under the model cooling curves generated for individual samples (Table 3). The "area" has units (°C s) and is obtained by fitting each model curve to a polynomial expression and integrating the expression between the limits T_e and T_g (Fig. 8B). The parameter is a measure of the relative time each sample resides at conditions suitable for welding (e.g., sintering) and viscous compaction. Computed values for samples from section SCC-1 of the Bandelier Tuff are reported in Table 3 for both the anhydrous and hydrous melts (Fig. 8B). The magnitude of the integrated area is a reflection of the cooling history (e.g., depth position) of each sample. The total variation between samples is 1 to 2 orders of magnitude. However, the value of T_g chosen (e.g., hydrous vs. anhydrous) also

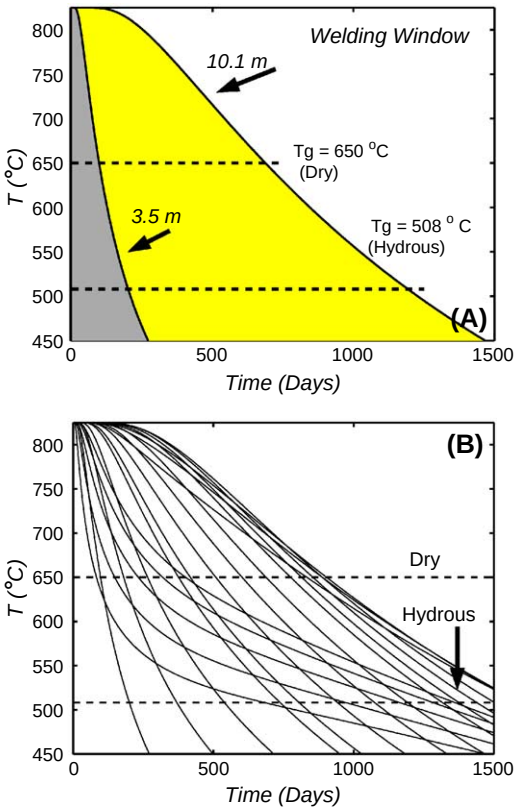

Fig. 8. The concept of welding window and residence time. (A) Model cooling curves predicted for depths (3.5 m and 10.1 m) corresponding to two samples from the SCC-1 section of Bandelier Tuff. The area under each curve, between the original emplacement temperature (T_e) and T_g, is a measure of the residence time at temperatures consistent with welding. (B) The model cooling curves for all 20 samples are plotted as T (°C) vs. time (days) and compared to the values of T_g for a anhydrous and hydrous melt (Table 3).

causes up to an order of magnitude variation in this parameter.

6. Rheological model for welding

The strain accumulated in pyroclastic deposits during the welding process results from the combined effects of sintering and viscous compaction of particles at temperatures in excess of T_g and the mechanical compaction of rigid particles (e.g., $T<T_g$; Sheridan and Ragan, 1976; Sheridan and Wang, 2005—this issue). These components are somewhat analogous to the creep and densification processes that govern hot pressing of glass and ceramic powders (e.g., Rahaman et al., 1987). Commonly, the total strain observed in such experiments is ascribed to two components: a component that supports flow and represents mainly pure shear strain (creep strain) and a component due to volume strain via porosity loss (densification; e.g., Venkatachari and Raj, 1986; Rahaman et al., 1987; Ducamp and Raj, 1989; Sura and Panda, 1990). In the ceramic materials, porosity is consigned to the matrix alone and, thus, total strain involves both volume-conserving pure shear strain (creep) and volume strain (densification). The deformation of natural pyroclastic materials is fundamentally different in that the deformation involves particles that are themselves porous and the deformation is dominantly by volume strain until all porosity is lost (Quane, 2004; Quane and Russell, 2005—this issue).

We describe the total observed strain in samples of welded pyroclastic material in terms of a viscous component (e.g., ε_v) and a mechanical component (e.g., ε_m):

$$\varepsilon_T = \varepsilon_v + \varepsilon_m. \quad (4)$$

We view these two components of deformation as operating in parallel and independently (Poirier, 1985; He et al., 2002). The rheology of the time-dependent viscous component of deformation is described by:

$$\sigma = \eta \frac{d\varepsilon_v}{dt} \quad (5)$$

where σ is the stress due to lithostatic loading and η is the viscosity of the pyroclastic deposit which implies:

$$d\varepsilon_v = \frac{\sigma}{\eta} dt. \quad (6)$$

The work of Rahaman et al. (1987), Ducamp and Raj (1989), Sura and Panda (1990), and Quane and Russell (2005—this issue) support the proposition that the effective viscosity of porous mixtures of ceramic materials during high-temperature deformation can be modeled as:

$$\eta = \eta_o \exp\left\langle \frac{-\alpha\phi}{1-\phi} \right\rangle \quad (7)$$

where η_o is the projected viscosity of the material at zero porosity and α is an adjustable fit parameter

determined by experimental study. Substitution of Eq. (7) into Eq. (6) yields:

$$d\varepsilon_v = \frac{\sigma}{\eta_o}\exp\left\langle \frac{\alpha\phi}{1-\phi}\right\rangle dt \quad (8)$$

However, earlier we established equivalence between changes in porosity and integrated strain (Eq. (2)) which allows Eq. (8) to be rewritten as:

$$d\varepsilon_v = \frac{\sigma}{\eta_o}\exp\left\langle \frac{\alpha[\phi_o-\varepsilon_v]}{1-\phi_o}\right\rangle dt. \quad (9)$$

Separation of variables provides the following integral expressions

$$\int \frac{\sigma}{\eta_o}dt = \int \exp^{\left\langle\frac{-\alpha[\phi_o-\varepsilon_v]}{1-\phi_o}\right\rangle} d\varepsilon_v. \quad (10)$$

The variable η_o is treated as constant. This simplification assumes that variations in the viscosity of the material at zero porosity (η_o) due to temperature are small relative to the overall variations in viscosity due to porosity loss. Clearly, cooling will cause an increase in η_o; however, much of the porosity loss can occur prior to the deposit cooling substantially. Integration of Eq. (10) provides an expression relating load, strain, and time during viscous compaction of a porous medium:

$$\frac{\sigma\Delta t}{\eta_o} = \frac{(1-\phi_o)}{\alpha}\exp^{\left\langle\frac{\alpha(\varepsilon_v-\phi_o)}{1-\phi_o}\right\rangle} + C. \quad (11)$$

The integration constant C is solved for by requiring the viscous component of accumulated strain to be zero at Δt=0:

$$C = \frac{-(1-\phi_o)}{\alpha}\exp^{-\left\langle\frac{\alpha\phi_o}{1-\phi_o}\right\rangle} \quad (12)$$

yielding:

$$\frac{\alpha\sigma\Delta t}{\eta_o(1-\phi_o)} = \exp^{\left\langle\frac{\alpha(\varepsilon_v-\phi_o)}{1-\phi_o}\right\rangle} - \exp^{\left\langle\frac{-\alpha\phi_o}{1-\phi_o}\right\rangle}. \quad (13)$$

Rearranging Eq. (13) provides a constitutive relationship that relates ε_v to original porosity, framework viscosity, load, and time:

$$\varepsilon_v = \frac{(1-\phi_o)}{\alpha}\ln\left\{\frac{\alpha\sigma\Delta t}{\eta_o(1-\phi_o)} + \exp^{\frac{-\alpha\phi_o}{(1-\phi_o)}}\right\} + \phi_o. \quad (14)$$

The mechanical component of strain (ε_m) is assumed to be linearly proportional to load:

$$\sigma = E(1-\phi_o)\varepsilon_m \quad (15)$$

where E is the Young's modulus for the non-porous framework material under uniaxial compression (Quane and Russell, 2003). Rearrangement of Eq. (15) and combining the terms for viscous and mechanical strain yields:

$$\varepsilon_T = \frac{(1-\phi_o)}{\alpha}\ln\left\{1+\frac{\alpha\sigma\Delta t}{\eta_o(1-\phi_o)}\exp^{\frac{\alpha\phi_o}{(1-\phi_o)}}\right\} + \frac{\sigma}{E(1-\phi_o)} \quad (16)$$

which accommodates time-dependent (1st term) and time-independent (2nd term) deformational processes operating in parallel (Poirier, 1985). The relationship expressed by Eq. (16) contains knowns and unknowns. The knowns derive from measurements of physical properties and the results of our thermal modeling and include σ, ε_T, ϕ_o, and Δt (Tables 2 and 3). Unknowns include η_o, α, and E.

We turn to results from high-temperature compaction experiments to constrain the coefficient α (Fig. 9).

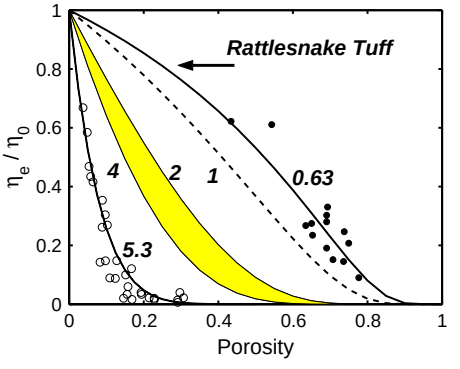

Fig. 9. Models for the rheology of porous materials deformed under an applied load at elevated temperatures based on the work of Rahaman et al. (1987) and Sura and Panda (1990). Model curves show how porosity affects the viscosity of the material, expressed as the ratio of effective viscosity (η_e) to viscosity of the melt (e.g., non-porous; η_o). Curves are shown for different values of α deriving from: (i) high-T deformation experiments on cores of glass beads (○, α=5.3; Quane and Russell, 2005—this issue), (ii) compaction experiments on ceramic powders (e.g., Rahaman et al., 1987), (iii) high-T deformation experiments on cores of ash from the Rattlesnake tuff (●, α=0.63; Quane, 2004), and (iv) α=1.0.

Sintering experiments on glass and ceramic powders under an applied load and elevated temperatures suggest values of α between 2 and 4 (Rahaman et al., 1987; Sura and Panda, 1990). Quane and Russell (2005—this issue) performed a series of high-T deformation experiments (535–650 °C) on unconfined cores of soda-lime glass beads (○; Fig. 9) and fitted their data to an α value of 5.3. More recently, Quane (2004) performed a similar set of experiments on fabricated cores of natural ash (washed and sieved) collected from the Rattlesnake Tuff (e.g., Streck and Grunder, 1995; Grunder et al., 2005—this issue). The experiments on the natural material imply a substantially different value for α (0.63) which may be largely ascribed to differences in the porosities of the synthetic (0%) and natural (≫0%) particles (e.g., pyroclasts).

7. Model optimization

We now use the data collected on samples from section SCC-1 to constrain the values of η_o and E. The optimization essentially provides a rheological model for welding of the Bandelier Tuff and elucidates the proportion of strain that is attributable to viscous compaction or mechanical compaction. We obtain estimates on the model parameters by solving a system of equations:

$$\frac{(1-\phi_o)}{\alpha}\ln\left\{1+\frac{\alpha\sigma_i\Delta t_i}{\eta_o(1-\phi_o)}\exp^{\frac{\alpha\phi_o}{(1-\phi_o)}}\right\} + \frac{\sigma}{E(1-\phi_o)} = \varepsilon_i \quad (17)$$

There is one equation for each sample (N=20) and values of ε_i, σ_i, and Δt_i for individual samples are: (a) the total strain calculated from porosity (e.g., Table 1), the calculated lithostatic load (Table 3), and the model residence times at $T>T_g$ (Table 3), respectively. Solving the system of equations (Eq. (17)) provides estimates of the apparent viscosity of the deposit at zero porosity (η_o) and Young's modulus of the pyroclastic material at zero porosity (E).

The optimization of the system of equations has been performed for a variety of model scenarios. Results are tabulated and illustrated in Table 4 and Fig. 10, respectively. The first model (Model 1 in Table 4) ascribes all observed strain to mechanical compaction (ε_v=0). The one-parameter solution estimates Young's modulus to be 1.95 MPa (η_o is unconstrained) but, is unable to capture the non-linear aspects of the strain-depth relationship (Fig. 10A). The next models allow for both viscous and mechanical compaction and use different values of α (5.3 and 0.63). There is little difference in results, but the models that use α=0.63 are favored because the original experiments are directly relevant to compaction of natural materials. Furthermore, models using an α of 0.63 provide a slightly better fit to the data (cf. Models 3 vs. 5; Table 4). The modeling also explores the effects of changing T_g implied by different H_2O contents (e.g., anhydrous vs. hydrous). Higher H_2O contents cause a depression in T_g which increases the effective residence time in the welding window (e.g., Δt_i in Eq. (17)).

Fig. 10B shows results from two models (Models 4 vs. 5; Table 4). The solid lines show the model components of strain due to viscous compaction (ε_v), mechanical compaction (ε_m), and the combination (ε_t) assuming an α of 0.63 and a hydrous Bandelier Tuff (e.g., lower T_g). The model fits the data well (Table 4) suggesting that, at the base of the deposit, mechanical compaction accounts for more than half of the total strain. The proportion of strain assigned to viscous compaction (ε_v) increases with depth to 20 m where it peaks at about 40% of the total strain. This peak in viscous compaction coincides with the peak in total strain, implying that the maximum intensity in deformation (e.g., welding intensity) depends mainly on viscous compaction (e.g., temperature and viscosity) rather than mechanical compaction (e.g., load).

The dashed lines are the results of the optimization when the anhydrous parameters (e.g., higher T_g and lower Δt_i) are used. The anhydrous models have increased proportions of mechanical strain at the expense of decreased amounts of viscous strain. An anhydrous pyroclastic deposit has a smaller (T_e-T_g) interval which translates into smaller times of residence in the welding window and, thus, less time to support viscous deformation. The optimal solutions based on an anhydrous Bandelier Tuff cannot reproduce the peak strains found in the lower third of the section. This is because the peak in welding intensity (e.g., strain) is mainly reached through viscous (time-dependent) compaction.

Table 4
Values of optimal parameters (E_o and η_o) returned from fitting deformation models to field data from Bandelier tuff

		Model 1	Model 2 Anhydrous	Model 3 Hydrous	Model 4 Anhydrous	Model 5 Hydrous	Model 6 Hydrous			
α		–	5.3	5.3	0.63	0.63	0.63			
E (MPa)		1.95	3.24	10.9	2.55	3.18	6.75			
$\log(\eta_o)$ Pa s		–	16.36	16.16	14.42	14.64	14.53			
γ		–	–	–	–	–	0.05			
Depth (m)	ε (ϕ)	ε (1)	ε (2)	ε (3)	ε (4)	ε (5)	ε_o	ε_m	ε_v	ε (6)
0	0.000	0.005	0.003	0.001	0.003	0.003	0.05	0.001	0.000	0.051
3.51	0.080	0.053	0.042	0.040	0.043	0.036	0.05	0.015	0.005	0.070
4.81	0.118	0.071	0.066	0.076	0.062	0.054	0.05	0.021	0.013	0.083
5.87	0.118	0.087	0.090	0.107	0.080	0.071	0.05	0.025	0.023	0.098
7.02	0.135	0.104	0.120	0.140	0.103	0.093	0.05	0.030	0.037	0.117
7.40	0.151	0.110	0.130	0.151	0.111	0.100	0.05	0.032	0.043	0.124
8.24	0.160	0.123	0.154	0.171	0.131	0.118	0.05	0.036	0.055	0.140
9.15	0.185	0.138	0.177	0.191	0.154	0.139	0.05	0.040	0.070	0.159
10.07	0.174	0.152	0.200	0.209	0.177	0.159	0.05	0.044	0.085	0.178
11.13	0.217	0.170	0.225	0.227	0.206	0.184	0.05	0.049	0.102	0.201
11.74	0.231	0.180	0.239	0.237	0.222	0.199	0.05	0.052	0.113	0.215
12.50	0.240	0.193	0.254	0.248	0.242	0.216	0.05	0.056	0.125	0.231
13.42	0.260	0.209	0.272	0.261	0.264	0.238	0.05	0.060	0.140	0.250
15.32	0.265	0.243	0.303	0.283	0.307	0.281	0.05	0.070	0.168	0.288
15.93	0.294	0.254	0.312	0.289	0.319	0.294	0.05	0.073	0.176	0.299
17.08	0.317	0.275	0.326	0.299	0.337	0.318	0.05	0.079	0.189	0.318
20.43	0.358	0.341	0.328	0.316	0.336	0.367	0.05	0.098	0.200	0.348
20.96	0.350	0.351	0.322	0.316	0.332	0.370	0.05	0.101	0.196	0.347
21.57	0.327	0.363	0.312	0.313	0.326	0.369	0.05	0.105	0.185	0.340
22.26	0.271	0.376	0.298	0.305	0.319	0.361	0.05	0.109	0.165	0.324
22.95	0.271	0.388	0.283	0.285	0.316	0.338	0.05	0.112	0.127	0.289
χ^2		20.0	30.4	14.5	0.57	0.56				0.02

Models vary depending on values of α and whether ignimbrite is treated as anhydrous or hydrous. Model 6 incorporates an additional adjustable parameter (see text). Value of χ^2 is sum of weighted residuals.

Our last model is a three-parameter solution created by allowing for a finite value of initial strain (γ) in addition to the strain induced by mechanical and viscous compaction:

$$\varepsilon_T = \varepsilon_v + \varepsilon_m + \gamma. \quad (18)$$

The results are illustrated in terms of the individual contributions to the total observed strain in Fig. 10C (Model 6; Table 4). This model allows for a fixed amount (0.05) of initial strain and requires a reduction in mechanical compaction (ε_m) and a corresponding increase in the proportion of viscous deformation (ε_v). This model offers a marginally better fit to the data (e.g., Fig. 10C, D) simply because of the extra adjustable parameter and requires a substantially larger value of E (6.8 vs. 3.2 MPa). The values of E returned by these models are within the ranges of uniaxial compressive strengths (2–12 MPa) measured by Quane and Russell (2003) on samples of Bandelier Tuff.

If this model is accepted, there are several possible explanations for the finite positive value of γ. Firstly, the observed strain may incorporate a component of strain that accumulated during emplacement (e.g., agglutination and compaction: Sheridan and Ragan, 1976; Branney and Kokelaar, 1992). Secondly, if a larger portion of the pyroclastic section is missing, the model values of load would be too small and the mechanical compaction potentially underestimated. Lastly, uncertainties in the thermal modeling (e.g., $[T-T_g]$) affect the values of Δt_i. If the estimated residence times are small, then the optimal values of ε_o tend to zero or

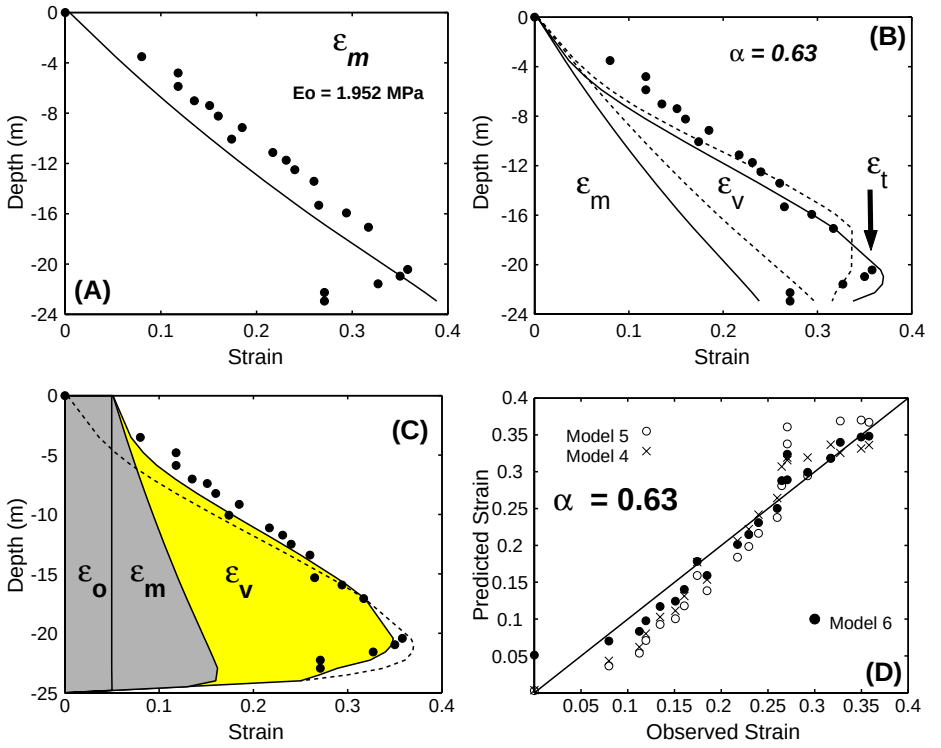

Fig. 10. Model results derived from fitting Eq. (17) to values of strain calculated for samples of Bandelier tuff. (A) Results for model where all strain (ε_m) is attributed to mechanical compaction (—) compared to observed values of strain (●). (B) Optimal fits of model equation assuming a value of α=0.63 for hydrous (—) and anhydrous (- - -) pyroclastic material. Individual lines partition the total model strain (ε_t) into components of strain ascribed to mechanical (ε_m) and viscous (ε_v) compaction. (C) Model results for a three parameter solution allowing for a finite value of initial strain (ε_o) in addition to the strain accumulating from mechanical and viscous compaction. Dashed line shows predicted total strain for two parameter solution (Fig. 10B; hydrous case). (D) Observed values of strain compared to model values (see Table 4).

even negative numbers. If the values of Δt_i are increased (or overestimated) then the magnitude of ε_o will increase accordingly.

8. The welding window

We adopt two dimensionless numbers (Q_A and Q_B) to explore the concept of a welding window and make a map of welding potential. Under favorable load and temperature conditions welding processes proceed; outside the welding window compaction and deformation are limited by absence of a lithostatic load, or by low emplacement temperatures, or by both. The first dimensionless parameter Q_A is given by:

$$Q_A = \frac{A}{[T_e - T_g]\tau} \tag{19}$$

where A is the integrated area (°C s) under the cooling history curve between the limits T_e and T_g (Table 4). The denominator is the product of the temperature interval $[T_e - T_g]$ and a characteristic time (τ) for viscous compaction under atmospheric loading. The value of τ is a constant computed from:

$$\tau = \frac{\varepsilon \eta_{T_g}}{\sigma} \tag{20}$$

for 100% strain (ε=1), atmospheric loading (σ=10^5 Pa) and a melt viscosity at T_g (η_{T_g}=$10^{12.5}$ Pa s). The parameter Q_A essentially compares the cooling history path (A) of each sample to a constant that is characteristic of the entire deposit (denominator).

The second dimensionless variable (Q_B) is defined as:

$$Q_B = \frac{\sigma t}{\eta_{T_g}} \tag{21}$$

where σ is lithostatic load at a specific depth, t is the total time for cooling from T_e to T_g and η_{T_g} is the melt viscosity at T_g. The numerator of Q_B is unique for each sample whereas the denominator is a limiting constant (e.g., $10^{12.5}$).

Values of Q_A and Q_B are calculated for each sample (Table 4) and plotted against depth in Fig. 11A. The calculations are made assuming the melt is anhydrous (lower limit) or hydrous (upper limit). Both Q_A and Q_B increase to a maximum below the midpoint of the section (Fig. 11A) because of the asymmetric cooling profile of the ignimbrite and the effects of increasing lithostatic load, respectively. The peak values do not occur at the same depth. Plotted against each other (Fig. 11B), the values of Q_A and Q_B define a loop. Values of Q_A and Q_B are near zero at the top and bottom of the section but increase in the interior of the unit as cooling time increases and the numerator of each dimensionless number begins to dominate. Samples near the base show greater increases in Q_B than in Q_A because of the effects of load.

Until we collect more data from other welded pyroclastic deposits, we propose a value of 1 as a critical threshold for each of these parameters. Below unity, the denominator dominates; individual sample properties (numerator) are numerically less than the limiting relaxation time-scales of the deposit. Conversely, values greater than 1 indicate that the sample attributes are dominant over the limiting trait of the deposit. These thresholds cut the map of welding potential (Fig 11B) into 4 quadrants. Welding processes operate efficiently where both dimensionless parameters exceed 1 (Quadrant *W*; Fig. 11B) but are not viable where neither Q_A nor Q_B exceed 1 (*U*; Fig. 10B). Two other quadrants feature mixed dimensionless numbers: one parameter is greater than 1 and the other is less than 1. These quadrants are domains where welding and compaction are driven thermally but without the aid of lithostatic load (W_T; Fig. 10B) or are driven mainly by lithostatic load (W_L; Fig. 10B). The former situation may be realized in relatively thin pyroclastic deposits (fall or flow), which are emplaced at temperatures well above their glass transition temperatures ($T_e \gg T_g$), such as in proximal facies of some air fall deposits (e.g., Sparks and Wright, 1979; Kamata et al., 1993). The latter case may be found in very thick accumulations of

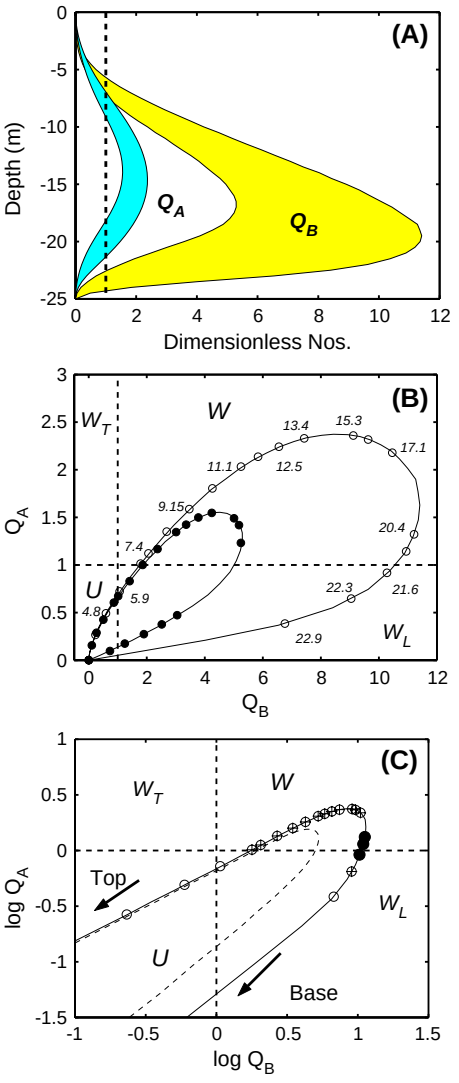

Fig. 11. Dimensionless numbers Q_A and Q_B used to characterize the welding window in cooling ignimbrite (Table 3). (A) Distribution of calculated dimensionless numbers Q_A and Q_B plotted against depth. Shaded fields denote the range in Q_A and Q_B due to anhydrous vs. hydrous melt. (B) Welding window based on dimensionless numbers Q_A and Q_b and defining zones of no welding (*U*), welding driven by temperature (W_T) or by load (W_L), or both (*W*). Curves are for anhydrous (solid) or hydrous (open) melt; labels are sample depths for hydrous situation. (C) Results plotted as log Q_A vs. log Q_B for anhydrous (- - -) and hydrous (—) ignimbrite. Individual samples (circles) are shown for hydrous ignimbrite. Samples between depths of 7–20 m plot in the *W* zone; samples from greater depths fall in zone W_L; the most shallow samples are in zone *U*. Crosses denote samples where viscous compaction dominates (ε_v: ε_m ratios $\gg$1.0; Fig. 10). Filled circles are samples showing highest welding intensity (Table 1; Rank III).

pyroclastic deposits that are emplaced at conditions of $T_e \approx T_g$ (e.g., Ragan and Sheridan, 1972; Sheridan and Ragan, 1976; Wilson and Hildreth, 2003), Merapi-style block and ash flow deposits (e.g., Abdurachman et al., 2000; Voight and Davis, 2000), or in volcanic conduits (Tuffen et al., 2003).

The samples of Bandelier Tuff describe two loops in the map of welding potential (Fig. 11B) depending on whether the rhyolitic tuff is treated as anhydrous or hydrous. The anhydrous end-member path allows for only minor welding in the middle to lower portions of the section. At depths greater than 15 m, welding would be driven by lithostatic load (W_L quadrant) because of the relatively high T_g of the anhydrous melt. The addition of H_2O decreases the effective T_g substantially and, therefore, the predicted distribution of welded samples increases markedly. More than half the samples (those spanning the interval 7–20 m) fall into the welding quadrant (W). Samples below 20 m are also within the welding window (W_L) because of the influence of load. Samples from the upper 5 m and from the very base of the unit plot in the unwelded quadrant and have little potential for welding. Ultimately, this map for welding potential (Fig. 11B) could be refined by incorporating field and lab data from a wider variety of welded pyroclastic deposits. Such an exercise could provide a more robust calibration of the critical threshold values for no welding (U), welding (W), and welding driven by temperature (W_T) or load (W_L).

Lastly, we compare results derived from the inverse modeling (ε_v and ε_m; Table 4 and Fig. 10) to the values of Q_A and Q_B calculated for the Bandelier Tuff. The logarithms of the dimensionless parameters are plotted (Fig. 11C) to better view values that were originally closely spaced at the origin (e.g., Fig. 11B). We suggest that high values of Q_A should correlate with high values of ε_v and Q_B with values of ε_m. Specifically, we would expect that deposits which intersect the W_T quadrant should be dominated by viscous compaction ($\varepsilon_v \gg \varepsilon_m$) and deposits that plot within the W_L quadrant should be dominated by mechanical compaction ($\varepsilon_m \gg \varepsilon_v$). Welded bodies that plot in the W quadrant are expected to feature significant amounts of both mechanical and viscous compaction. Our inverse modeling of the Bandelier Tuff (Model 6; Table 4) suggests that generally $\varepsilon_m \cong \varepsilon_v$ except between 7 and 20 m where the ratio of ε_v to ε_m is ≥ 1 (Fig. 11C, crossed circles. The majority of these samples plot, as predicted, within the W quadrant. As sample depth increases, the role of load increases and the ratio of ε_v to ε_m decreases to less than 1.0.

9. Summary

We have presented a constitutive relationship for strain resulting from welding and compaction of pyroclastic materials. The model assumes that the observed strain results from mechanical and viscous compaction. The constitutive relationship allows prediction of strain as a function of time for a given load and original porosity. The model also requires knowledge of three physical constants: α, η_o, and E. We adopted a value of 0.63 for α based on recent experimental work (Quane and Russell, 2005—this issue; Quane, 2004) and used the strain distribution in the Bandelier Tuff to fix the values of η_o and E at $10^{14.6}$ Pa s and 3–7 MPa, respectively.

The optimized constitutive relationship was used to compute the proportions of strain due to viscous and mechanical compaction as a function of position (e.g., depth) in the Bandelier Tuff. Mechanical compaction increases with depth from zero near the top of the section to a maximum of 38% at the base. Viscous compaction dominates the lower two-thirds of the section and the maximum in viscous compaction (60%) coincides with the peak in welding intensity. This suggests that the maximum intensity in welding is ultimately controlled more by the magnitude of $[T_e - T_g]$ than load.

Dimensionless numbers (Q_A and Q_B) were introduced to create a map of welding potential. The denominator to each dimensionless parameter is a constant for a given deposit; the numerator varies depending on the sample position. Our preliminary analysis suggests that unity be adopted as the critical values of Q_A and Q_B and this creates four quadrants on the map of welding potential. The quadrants coincide with (i) no welding ($\varepsilon_v \cong \varepsilon_m \cong 0$), (ii) welding and compaction driven by temperature ($\varepsilon_v > \varepsilon_m$) or by (iii) gravitational loading ($\varepsilon_m > \varepsilon_v$), and (iv) welding aided by temperature and load ($\varepsilon_v \cong \varepsilon_m > 0$).

Acknowledgments

The authors greatly appreciate the support of staff at Los Alamos National Laboratory (EES-6), especially Don Krier, during the field sampling program. Financial support derived from The Natural Sciences and Engineering Research Council of Canada (Discovery Grants program to JKR) and the Geological Society of America (Graduate Student Research Grant to SQ). We are also indebted to many colleagues for frank and free exchange of ideas prior to and during the preparation of this manuscript, including: Anita Grunder, Lori Kennedy, Hugh Tuffen, Alison Rust, and Greg Dipple. We especially acknowledge the efforts of Jim Gardner and Daniele Giordano who provided thorough reviews of the original manuscript; their comments provided a basis for improving the clarity and consistency of our arguments.

References

Abdurachman, E.K., Bourdier, J.L., Voight, B., 2000. Nuees ardentes of 22 November 1994 at Merapi Volcano, Java, Indonesia. J. Volcanol. Geotherm. Res. 100, 345–361.

Bierwirth, P.N., 1982. Experimental Welding of Volcanic Ash. Unpublished B.Sc. Thesis, Monash University.

Boyd, F.R., 1961. Welded tuffs and flows in the rhyolite plateau of Yellowstone Park, Wyoming. Geol. Soc. Am. Bull. 72, 387–426.

Branney, M.J., Kokelaar, P., 1992. A reappraisal of ignimbrite emplacement; progressive aggradation and changes from particulate to non-particulate flow during emplacement of high-grade ignimbrite. Bull. Volcanol. 54, 504–520.

Broxton, D.E., Reneau, S.L., 1995. Stratigraphic nomenclature of the Bandelier tuff for the environmental restoration project at Los Alamos National Laboratory. Los Alamos Nat Lab Rep, LA-13010-MS: 21 pp.

Carslaw, H.S., Jaeger, J.C., 1959. Conduction of Heat in Solids. Oxford University Press, New York, 510 pp.

Dingwell, D.B., Webb, S.L., 1989. Structural relaxation in silicate melts and non-Newtonian melts rheology in geologic processes. Phys. Chem. Miner. 16 (5), 508–516.

Dingwell, D.B., Webb, S.L., 1990. Relaxation in silicate melts. Eur. J. Mineral. 2, 427–449.

Ducamp, V.C., Raj, R., 1989. Shear and densification of glass powder compacts. J. Am. Ceram. Soc. 72, 798–804.

Dunnet, D., 1969. A technique of finite strain analysis using elliptical particles. Tectonophysics 7, 117–136.

Elliot, D., 1970. Determination of finite strain and initial shape from deformed elliptical objects. Geol. Soc. Am. Bull. 81, 2221–22236.

Friedman, I., Long, W., Smith, R.L., 1963. Viscosity and water content of rhyolite glass. J. Geophys. Res. 68, 6523–6535.

Giordano, D., Dingwell, D.B., Romano, C., 2000. Viscosity of a Teide phonolite in the welding interval. In: Marti, J., Wolff, J.A. (Eds.), The Geology and Geophysics of Tenerife, J. Volcanol. Geotherm. Res. 103, 239–245.

Giordano, D., Nichols, A.R., Dingwell, D.B., 2005. Glass transition temperatures of natural hydrous melts: a relationship with shear viscosity and implications for the welding process. J. Volcanol. Geotherm. Res. 142, 105–118 (this issue).

Goff, F., 1995. Geologic map of technical area 21. In: Broxton, D.E., Eller, P.G. (Eds.), Earth Science Investigations for Environmental Restoration—Los Alamos Laboratory Technical Area 21, Los Alamos National Laboratory report LA-12934-MS.

Gottsmann, J., Dingwell, D.B., 2001. Cooling dynamics of spatter-fed phonolite obsidian flows on Teneriefe, Canary Islands. J. Volcanol. Geotherm. Res. 105, 323–342.

Grunder, A.L., Russell, J.K., 2005. Welding processes in volcanology: insights from field, experimental and modeling studies. J. Volcanol. Geotherm. Res. 142, 1–9.

Grunder, A.L., Laporte, D., Druitt, T.H., 2005. Experimental and textural investigation of welding: effects of compaction, sintering, and vapor-phase crystallization in the rhyolitic Rattlesnake Tuff. J. Volcanol. Geotherm. Res. 142, 89–104.

Guest, J.E., Rogers, P.S., 1967. The sintering of glass and its relationship to welding in ignimbrites. Proc. Geol. Soc. London 1641, 174–177.

He, W., Hajash, A., Sparks, D., 2002. A model for porosity evolution during creep compaction of sandstones. Earth Planet. Sci. Lett. 197, 237–244.

Kamata, H., Suzukikamata, K., Bacon, C.R., 1993. Deformation of the Wineglass welded tuff and the timing of caldera collapse at Crater Lake, Oregon. J. Volcanol. Geotherm. Res. 56, 253–266.

Kobberger, G., Schmincke, H.U., 1999. Deposition of rheomorphic ignimbrite D (Mogan Formation) Gran Canaria, Canary Islands, Spain. Bull. Volcanol. 60, 465–485.

Krier, D., Caporuscio, F., Lavine, A., Gardner, J., 1998. Stratigraphy and geologic structure at the SCC and NISC building sites, technical area 3, Los Alamos National Laboratory, New Mexico, Los Alamos National Laboratory technical report LA-13507-MS.

Miller, T.F., 1990. A numerical model of volatile behavior in nonwelded cooling pyroclastic deposits. J. Geophys. Res. 95, 19349–19364.

Peterson, D.W., 1979. Significance of the flattening of pumice fragments in ash-flow tuffs. In: Chapin, C.E., Elston, W.E. (Eds.), Ash-flow Tuffs. Spec. Pap. Geol. Soc. Am., 180, 195–204.

Philpotts, A.R., 1990. Principles of Igneous and Metamorphic Petrology. Prentice-Hall, 498 pp.

Poirier, J.P., 1985. Creep of Crystals: High Temperature Deformation Processes in Metals, Ceramics and Minerals. Cambridge University Press, Cambridge, 260 pp.

Quane, S.L., 2004. Welding in Pyroclastic Deposits. PhD thesis. University of British Columbia, 202 pp.

Quane, S.L., Russell, J.K., 2003. Rock strength as a metric of welding intensity in pyroclastic deposits. Eur. J. Mineral. 15, 855–864.

Quane, S.L., Russell, J.K., 2004. Ranking welding intensity in pyroclastic deposits. Bull. Volcanol.

Quane, S.L., Russell, J.K., 2005. Welding: insights from high-temperature analogue experiments. J. Volcanol. Geotherm. Res. 142, 67–87.

Ragan, D.M., Sheridan, M.F., 1972. Compaction of the Bishop Tuff, California. Geol. Soc. Am. Bull. 83, 95–106.

Rahaman, M.N., Jonghe, L.C., Scheree, G.W., Brook, R.J., 1987. Creep and densification during sintering of glass powder compacts. J. Am. Ceram. Soc. 70, 766–774.

Riehle, J.R., 1973. Calculated compaction profiles of rhyolitic ash-flow tuffs. Geol. Soc. Am. Bull. 84, 2193–2216.

Riehle, J.R., Miller, T.F., Bailey, R.A., 1995. Cooling, degassing and compaction of rhyolitic ash flow tuffs; a computational model. Bull. Volcanol. 57, 319–336.

Ross, C.S., Smith, R.L., 1961. Ash-flow tuffs their origin, geologic relations, and identification. U. S. Geol. Surv. Prof. Pap. 366, 81 pp.

Shaw, H.R., 1972. Viscosities of magmatic silicate liquids: an empirical model of prediction. Am. J. Sci. 272, 438–475.

Sheridan, M.F., Ragan, D.M., 1976. Compaction of ash-flow tuffs. In: Chilingarian, G.V., Wolf, K.H. (Eds.), Compaction of Coarse-Grained Sediments, vol. II. Elsevier, Amsterdam, Netherlands, pp. 677–717.

Sheridan, M.F., Wang, Y., 2005. Cooling and welding history of the Bishop Tuff in Adobe valley, California. J. Volcanol. Geotherm. Res. 142, 119–144.

Smith, R.L., 1960a. Ash flows. Geol. Soc. Am. Bull. 71, 795–841.

Smith, R.L., 1960b. Zones and zonal variations in welded ash flows. U. S. Geol. Surv. Prof. Pap. 354F, 149–159.

Smith, R.L., 1979. Ash-flow magmatism. In: Chapin, C.E., Elston, W.E. (Eds.), Ash-flow Tuffs. Spec. Pap. Geol. Soc. Am., 180, 5–27.

Smith, R.L., Bailey, R.A., 1966. The Bandelier Tuff; a study of ash-flow eruption cycles from zoned magma chambers. Bull. Volcanol. 29, 83–103.

Sparks, R.S.J., Wright, J.V., 1979. Welded air-fall tuffs. In: Chapin, C.E., Elston, W.E. (Eds.), Ash-flow Tuffs. Spec. Pap. Geol. Soc. Am., 180, 155–166.

Sparks, R.S.J., Tait, S.R., Yanev, Y., 1999. Dense welding caused by volatile resorption. J. Geol. Soc. (London) 156, 217–225.

Streck, M.J., Grunder, A.L., 1995. Crystallization and welding variations in a widespread ignimbrite sheet; the Rattlesnake Tuff, eastern Oregon, USA. Bull. Volcanol. 57, 151–169.

Sura, V., Panda, P., 1990. Viscosity of porous glasses. J. Am. Ceram. Soc. 73, 2697–2701.

Tuffen, H., Dingwell, D.B., Pinkerton, H., 2003. Repeated fracture and healing of silicic magma generate flow banding and earthquakes. Geology 31, 1089–1092.

Vaniman, D., Wohletz, K., 1990. Results of geological mapping/fractures studies, TA-55 area, Los Alamos National Laboratory Seismic Hazards Memo EES1-SH90-17.

Vaniman, D., Wohletz, K., 1991. Revisions to report EES1-SH90-17, Los Alamos National Laboratory Seismic Hazards Memo EES1-SH91-12.

Venkatachari, K.R., Raj, R., 1986. Shear deformation and densification of powder compacts. J. Am. Ceram. Soc. 69, 499–506.

Voight, B., Davis, M.J., 2000. Emplacement temperatures of the November 22, 1994 nuée ardente deposits, Merapi Volcano, Java. J. Volcanol. Geotherm. Res. 100, 371–377.

Wilson, C.J.N., Hildreth, W.H., 2003. Assembling an ignimbrite: mechanical and thermal building blocks in the Bishop Tuff. J. Geol. 111, 653–670.